PCCP

ROYAL SOCIETY OF CHEMISTRY

PAPER

View Article Online
View Journal | View Issue

Cite this: *Phys. Chem. Chem. Phys.*, 2025, **27**, 14966

Tetrel, nonconventional hydrogen bonds, and noticeable role of dispersion in complexes of fluoroform and carbon dichalcogenides†

Thanh-Nam Huynh,[a] Nguyen Thi Minh Nguyet,[b] Bui Duc Ai[b] and Nguyen Tien Trung *[bc]

Received 20th April 2025,
Accepted 25th June 2025

DOI: 10.1039/d5cp01508a

rsc.li/pccp

Weak noncovalent interactions in complexes between fluoroform and carbon dichalcogenides are explored using highly accurate quantum chemical calculations. Tetrel and hydrogen bonds stabilize these binary systems, with tetrel bonds dominating oxygen-containing complexes and hydrogen bonds prevailing in oxygen-free ones. Distinct characteristics are also found between the two groups in terms of electrostatic contributions. In the former, electrostatics play a secondary role, while in the latter, they are the least attractive term. In all complexes, dispersion interactions predominantly stabilize the most stable structures, with a more pronounced effect in complexes containing heavier chalcogens. The hydrogen bonds in all complexes are purely noncovalent in nature and exhibit blue shifts in the C–H stretching frequency to varying degrees. Detailed analysis of the linear hydrogen bonds in oxygen-containing complexes suggests that the blue shift is a short-range phenomenon, which results from a balance between blue-shift-driving exchange forces and red-shift-driving electrostatic interactions. Meanwhile, dispersion forces are found to exert red-shifting effects.

1 Introduction

Weak noncovalent interactions involving polarized C–H groups are particularly important for a wide range of chemical and biochemical activities, *e.g.*, protein folding,[1–7] enzyme catalysis,[7–9] and crystal packing,[10,11] to name a few. Despite their typical weak interaction strengths, the interplay of various interaction types and their cumulative effects could drive significant molecular transformations. Understanding the nature of noncovalent interactions is, therefore, of utmost necessity to elucidate the mechanisms of chemical and biochemical reactions and design materials with desired properties.

For decades, C–H···O hydrogen bond interactions have attracted significant attention, not only due to their critical role and prevalence in (bio)molecular systems[2,3,5] but also because they constitute an interesting subgroup of nonconventional blue-shifting hydrogen bonds.[12–21] Unlike conventional hydrogen bonds, which typically involve a lengthened C–H bond and a red shift in the corresponding vibrational frequency, blue-shifting hydrogen bonds are characterized by a shortened C–H bond and an increase in vibrational frequency. Some authors suggested that there is no fundamental distinction between these two types of hydrogen bonds.[12,14,17,22] Consequently, extensive efforts have been devoted to studying C–H···O systems to elucidate the nature of these interactions. Such interactions have been attributed to various factors, including electrostatic interactions,[13,15,20,21] Pauli repulsion,[16] polarization of the C–H bond coupled with an increase in s-character,[18] redistribution of electron density,[19] or C–H bond's polarization and the proton acceptor's gas-phase basicity.[23–26] Despite discrepancies among these explanations, a general consensus has emerged that the blue shift results from a delicate balance of opposing effects.

To explore this further, in addition to the conventional approach of analyzing equilibrium structures alone, the examination of hydrogen bond interactions along the potential energy surface, often paired with energy decomposition analyses, has been increasingly adopted to gain deeper insight into how this balance is achieved and how blue-shift behavior emerges. For instance, Mo *et al.*, using the block-localized wave function method, observed long-range blue-shift behavior in complexes of fluoroform with various bases, proposing that

[a] *Institute of Catalysis Research and Technology, Karlsruhe Institute of Technology, Hermann-von-Helmholtz-Platz 1, 76344 Eggenstein-Leopoldshafen, Germany*
[b] *Laboratory of Computational Chemistry and Modelling (LCCM), Quy Nhon University, 170 An Duong Vuong Street, Quy Nhon City 590000, Vietnam*
[c] *Faculty of Natural Sciences, Quy Nhon University, 170 An Duong Vuong Street, Quy Nhon City 590000, Vietnam. E-mail: nguyentientrung@qnu.edu.vn*

† Electronic supplementary information (ESI) available: Further information on molecular electrostatic potentials, noncovalent conformational sampling with CREST, AIM, SAPT, NBO analyses. See DOI: https://doi.org/10.1039/d5cp01508a

electrostatic interactions drive the blue shift.[20] This long-range phenomenon was also observed by Alabugin and colleagues.[18] In contrast, Mao and Head–Gordon revisited complexes of CHF_3 and argued that the blue shift is a short-range phenomenon.[27] These conflicting conclusions underscore the need for more comprehensive studies to better understand the blue-shift phenomenon. In this context, investigating weak interactions proves particularly valuable, as their subtle nature allows competing forces to stand out, providing clearer insights into the mechanisms governing hydrogen bond behavior.

Compared to C–H···O interactions, C–H-based interactions involving heavier chalcogens—such as sulfur, selenium, and tellurium—are significantly underrepresented, despite occasional claims that these atoms can serve as proton acceptors as effectively as oxygen.[28] The presence of C–H···S interactions has been increasingly documented through experimental and computational studies.[29–39] In these systems, the C–H bond exhibits weak red or blue shifts, depending on the nature of the hydrogen bond donors and acceptors. In contrast, research on C–H···Se[29,37,40–44] and C–H···Te[29,37] interactions is more limited, despite the former being experimentally identified as early as 1994.[40] Further studies of noncovalent interactions involving these heavier chalcogens could greatly enhance our understanding of their behavior and significance.

In this work, we aim to investigate the intermolecular interactions between fluoroform (CHF_3) and carbon dichalcogenides (XCY, where X, Y = O, S, Se, or Te), with a particular focus on C–H···X interactions. Specifically, we determine the geometries of the most stable complexes and analyze their stabilizing interactions, highlighting the role of nonconventional hydrogen bond C–H···X, particularly in the underrepresented C_{sp^3}–H···Se/Te. Moreover, we elucidate the role of energy components contributing to the blue and red shifts of the C–H stretching frequency. The CO_2 molecule has been a key subject for studying noncovalent interactions due to its promising potential as a green solvent[36,45,46] as well as for CO_2 sequestration applications.[47,48] Replacing one or both oxygen atoms in CO_2 with heavier chalcogens from the same group significantly alters the molecules's electronic structure due to reduced electronegativity and increased atomic size of the new atom. These more complex electronic structures create greater opportunities for various types of noncovalent interactions—such as hydrogen, halogen, chalcogen,[49] and tetrel bonds—to occur in their complexes with fluoroform,[45,50–54] causing difficulties in finding the lowest energy dimers. We address this issue by employing a multi-level optimization workflow, which initiates with an automatized noncovalent interaction conformational sampling, followed by refined optimizations at the MP2 level and single point energy calculations at the highly accurate CCSD(T) method. The characteristics of noncovalent interactions in the most stable complexes are revealed by atoms-in-molecules (AIM), natural bond orbitals (NBO), and high-order symmetry-adapted perturbation theory (SAPT) analyses. Further insight into the blue-shifting behavior and its nature is obtained by scanning potential energy surface for linear hydrogen bonding complexes of OCY molecules (Y = O, S, Se).

2 Computational details

All quantum mechanical calculations were performed using the Gaussian packages (version G16.A.03).[55] The conformational search for noncovalent complexes of fluoroform and carbon dichalcogenides were carried out using CREST workflow[56] (NCI mode) at GFN2-xTB level.[57] The refined geometry optimizations were done using the MP2 method in combination with the triple-ζ 6-311++G(3df,2pd) basis set, except for the Te-containing systems, where a basis set of aug-cc-pVTZ-PP was adopted for Te atoms. The chosen basis sets has been demonstrated to yield reliable results for systems containing similar elements.[26,58,59] Vibrational analyses were carried out in the same level of theory to confirm the optimized structures' minimum nature on the potential energy surface and to correct the zero-point vibrational energy (ZPE) *via*:

$$E_{\mathrm{ZPE}} = \sum_{i=1}^{3N-5/6} \frac{1}{2} h\nu_i, \tag{1}$$

in which, ν_i is the i-th vibrational frequency, N is the number of atoms in a given system. The non-covalent interactions investigated in this study are weak interactions, which fall in the range of 2–10 kJ mol^{-1}, thus requiring the best electronic structure descriptions. Hence, we performed single point energy and counterpoise[60] calculations at the CCSD(T)/6-311++G(3df,2pd) (aug-cc-pVTZ-PP for Te atoms where appropriate) to achieve interaction energies at coupled cluster accuracy and free from basis set superposition errors (BSSE). The ZPE-corrected interaction energy, ΔE_{int}, and the ZPE- and BSSE-corrected interaction energy, $\Delta E^{*}_{\mathrm{int}}$, present in the main text are defined as:

$$\Delta E_{\mathrm{int}} = \Delta E^{\mathrm{CC}}_{\mathrm{el}} + \Delta E^{\mathrm{MP2}}_{\mathrm{ZPE}}, \tag{2}$$

and

$$\Delta E^{*}_{\mathrm{int}} = \Delta E^{\mathrm{CC}}_{\mathrm{el}} + \Delta E^{\mathrm{MP2}}_{\mathrm{ZPE}} + E^{\mathrm{CC}}_{\mathrm{BSSE}}, \tag{3}$$

where $\Delta E^{B}_{A} \equiv E^{B}_{A,\mathrm{dimer}} - \sum E^{B}_{A,\mathrm{monomer}}$ is the difference in A energy (*i.e.*, E_{el}: electronic energy and E_{ZPE}: zero-point vibrational energy) between the dimer and sum of its constituting monomers calculated at theory level B, and $E^{\mathrm{CC}}_{\mathrm{BSSE}}$ is the BSSE at coupled cluster level.

Several complementary calculations and analyses were carried out to aid the understanding on the nature of the hydrogen bond under study. Molecular electrostatic potentials (MEPs) were derived from the MP2 densities and the mapped density plots were constructed at an isosurface of 0.001 a.u. using GaussView package. Additionally, the Multiwfn software[61] was used to locate the extrema on the MEP and compute their potential values. The topological properties of electron densities at critical points connecting the two monomers in a given interacting dimer were analyzed using the Bader's theory of atoms in molecule (AIM).[62] Such properties were obtained also from MP2 densities using AIMAll program.[63] Moreover, the natural bond orbital (NBO) analyses[64] were conducted at the ωB97X-D/aug-cc-pVTZ level using NBO 6.0 to investigate

the non-covalent interactions from a Lewis-like approach. Finally, contributions from physical forces, namely, electrostatic, exchange, dispersion, and induction, to the intermolecular interactions were obtained using an energy decomposition scheme within the symmetry-adapted perturbation theory (SAPT). High order SAPT analyses were done *via* the PSI4 package.[65] Additional supplementary figures and tables that further clarify the analyses and discussion presented hereafter are provided in the ESI.†

3 Results and discussion

3.1 Monomer properties

Much can be learned about the geometrical arrangement and stability of the noncovalently interacting complexes from the electrostatic potential surfaces of their constituent monomers.[66] For this purpose, we plot the MEP surfaces for the monomers of interest in Fig. 1 and present the values of selected extrema, $V_{s,min}$ and $V_{s,max}$, on these surface in Table 1. A color gradient from red to blue illustrates the transition from negative to positive potential values.

In the CHF_3 molecule, the electron-deficient region (positive potential) around the hydrogen atom is depicted as a blue area, which tends to interact with the electron-rich red regions (negative potential) of carbon dichalcogenides. Meanwhile, three negative regions are observed around the fluorine atoms, indicating electron-rich areas.

It is well established that oxygen exhibits distinct behavior compared to other chalcogens within the group. This difference is particularly evident in the MEP surfaces of oxygen-containing molecules (OCY, where Y = O, S, or Se), where the strong electron-withdrawing nature of oxygen renders the regions around the O atoms more negative, facilitating interactions with electrophilic hydrogen bond donors. Specifically, the MEP surfaces of OCY molecules feature a primary minimum along the extension of the C═O bond(s) and a band of maxima around the carbon atom. The $V_{s,min}$ decreases in the order OCSe < OCO < OCS, while $V_{s,max}$ increases in the order OCSe < OCS < OCO. For OCS and OCSe, a band of minima is observed around the Y atom, perpendicular to the molecular axis, alongside a maximum along the extension of the C–Y bond.

For oxygen-free molecules, minima appear as strips around the chalcogen atoms, perpendicular to the molecular axis, while maxima are located around the carbon atom and at the extensions of C–X and C–Y bonds. The $V_{s,max}$ at these bond extensions are comparable to those of OCY molecules and depend on the electronegativity of the chalcogen atom, while $V_{s,min}$ values are less negative than those of their OCY counterparts.

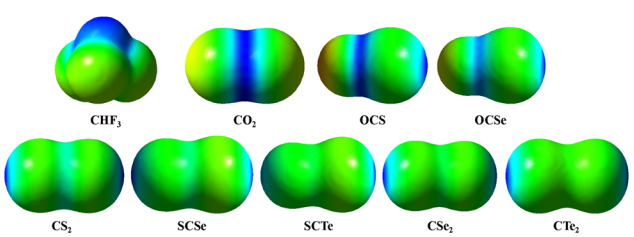

Fig. 1 Molecular electrostatic potential surfaces of the monomers at isosurface of 0.001 a.u.

Table 1 Potential values in kJ mol^{-1} at selected extrema on the electrostatic energy surface of isolated monomers

	Minimum		Maximum	
Molecule	Type	$V_{s,min}$	Type	$V_{s,max}$
CHF_3	F	−50	H	165
			σ-hole	140
OCO	O	−59	π-hole (C)	150
OCS	O	−64	σ-hole (S)	93
			π-hole (C)	83
OCSe	O	−54	σ-hole (Se)	113
			π-hole (C)	81
SCS	S	−9	σ-hole (S)	75
			π-hole (C)	23
SCSe	Se	−17	σ-hole (Se)	87
	S	−2	σ-hole (S)	81
			π-hole (C)	18
SCTe	Te	−21	σ-hole (Te)	116
			σ-hole (S)	82
			C	13
SeCSe	Se	−11	σ-hole (Se)	92
			C	11
TeCTe	Te	−13	σ-hole (Te)	114

3.2 Stable binary structures and types of interaction

The carbon dichalcogenides of interest in this study exhibit highly anisotropic electronic density populations (*cf.* Section 3.1). This gives rise to a number of possible noncovalently interacting structures of complexes formed by those dichalcogenides and fluoroform (CHF_3), making the manual preparation of guessed input structures based on chemical intuition a laborious and prone-to-error process. Therefore, in this study, a noncovalent interaction conformational sampling using the CREST workflow[56] in combination with the semi-empirical GFN2-xTB method[57] was applied. The practice has been shown effective in predicting exhaustive sets of possible geometries (see Section S1 of ESI†). The geometries of noncovalent complexes between CHF_3 and XCY (X, Y = O, S, Se, Te) were, then, refined using MP2/6-311++G(3df,2pd) method (MP2/aug-cc-pVTZ-PP for Te-containing structures). The interaction energies are corrected to the highly accurate CCSD(T) level of theory using the similar basis sets.

Fig. 2 presents the geometries of the most stable (nonlinear) hydrogen bond-involving complexes (**nL-1**, **2**, **3**) and those with only linear hydrogen bonding interactions (**L**), demonstrating the structural diversity, where several binding motifs are found. Their corresponding interaction energies at CCSD(T) level and interacting angles are tabulated in Table 2. All $F_3CH\cdots XCY$ structures in this study can be reasonably considered as "very weak" (hydrogen bonding) interaction complexes,[67] with interaction energy ranging between −6 and −3 kJ mol^{-1}. The interation energy of fluoroform with the carbon dichalcogenides is considerable less negative than that with more nucleophilic acceptors, such as, H_2O and NH_3,[16,18,19,21,68] highlighting

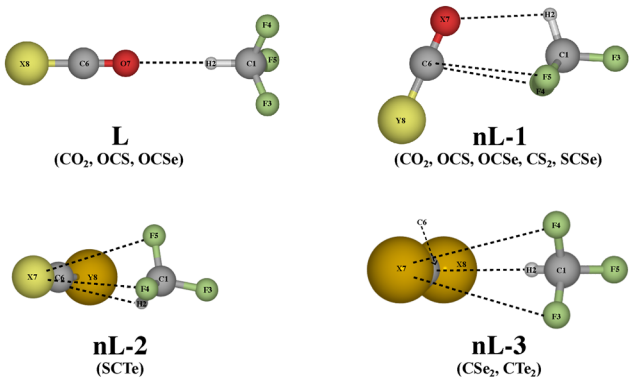

Fig. 2 The four geometrical motifs of the optimized noncovalently interacting $F_3CH\cdots XCY$ complexes, where X, Y are chalcogen atoms (O, S, Se, Te). The proton acceptors of complexes with stable structures exhibiting each motif are specified in the corresponding parentheses.

Table 2 Angular and energetic characteristics of hydrogen bonding complexes at the CCSD(T)/6-311++G(3df,2pd)//MP2/6-311++G(3df,2pd) level. ΔE_{int} and ΔE^{*}_{int} are ZPE-corrected and ZPE- and BSSE-corrected interaction energies, respectively, obtained *via* eqn (2) and (3). The suffices in parentheses denote the structures' binding motif (see Fig. 2)

Complex	∠C–H···X/C (deg)	ΔE_{int} (kJ mol^{-1})	ΔE^{*}_{int} (kJ mol^{-1})
$F_3CH\cdots OCO$(**L**)	180	−6.1	−4.1
$F_3CH\cdots OCS$(**L**)	180	−6.7	−4.4
$F_3CH\cdots OCSe$(**L**)	180	−6.1	−4.0
$F_3CH\cdots OCO$(**nL-1**)	101	−8.7	−5.2
$F_3CH\cdots OCS$(**nL-1**)	104	−9.0	−5.1
$F_3CH\cdots OCSe$(**nL-1**)	104	−8.4	−4.6
$F_3CH\cdots SCS$(**nL-1**)	116	−7.6	−3.3
$F_3CH\cdots SCSe$(**nL-1**)	123	−8.1	−4.2
$F_3CH\cdots SCTe$(**nL-2**)	124	−9.7	−4.4
$F_3CH\cdots SeCSe$(**nL-3**)	137	−8.1	−4.6
$F_3CH\cdots TeCTe$(**nL-3**)	144	−11.8	−5.8

the importance of employing the highly accurate CCSD(T) method. The MP_2 method performs well for oxygen-containing complexes but generally underestimates this quantity for their non-oxygen counterparts (Table S2, ESI†).

Based on the element acting as the proton acceptor (and NBO charge transfer, Table S3 and S4, ESI† as discussed later), we put the complexes of interest into two groups: $F_3CH\cdots OCY$ complexes (Y = O, S, Se), whose the tetrel bond C–F···C is the main interaction, supplemented by a C–H···O hydrogen bond, and $F_3CH\cdots XCY$ complexes (X, Y = S, Se, Te), where the C–H···X interaction dominates. All the most stable complexes of the first group adopt the **nL-1** motif where the C1–H2···O7 forms an angle of 101–104°. The H···O separation decreases from 2.688 to 2.646 to 2.645 Å as Y varies from O to S to Se, respectively. In addition to the hydrogen bond, two symmetrical C–F···C interactions are observed to stabilize the complexes. We also found less stable hydrogen bonding complexes that feature a linear binding motif (**L**) and high symmetry of C_{3v}, whose interaction energies are 0.6–1.1 kJ mol^{-1} more positive than their **nL-1** counterparts. It is, therefore, of great interest to elucidate the factors that drive the differences in stability and spectroscopic characteristics of the two $F_3CH\cdots OCY$ subgroups (hereafter referred to as nonlinear and linear $F_3CH\cdots OCY$, respectively).

In the second group, the $F_3CH\cdots SCS$ and $F_3CH\cdots SCSe$ complexes also assume the **nL-1** motif as the ground state structures. The **nL-2** motif is the most stable geometry of $F_3CH\cdots SCTe$ complex. A nearly isoenergetic structure of $F_3CH\cdots SCSe$ (**nL-1**) (energy difference of about 0.1 kJ mol^{-1}) takes on this interacting motif (Fig. S5, ESI†); however, this structure will not be considered later as their characteristics are highly similar to their counterpart. Different from **nL-1** and **nL-3** motifs (discussed later), where all hydrogen bond-involved atoms lies on the plane formed by the XCY linear molecule and CHF_3's carbon atoms, the C–H bond in **nL-2** complexes, instead, forms an angle of ∼40° with the plane, pointing toward the less electronegative X atom (or more correctly toward the negative electrostatic potential belt, see Fig. 1). The last motif is the most stable geometry for the $F_3CH\cdots SeCSe$ and $F_3CH\cdots TeCTe$ complexes. This corresponds to an arrangement of the two monomers similar to **nL-1**, but the C–H···C and C–F···X interactions form instead. The C–H···C angles are larger than those with **nL-1** motif by roughly 40. We note that a linear configuration involving only hydrogen bonding interaction cannot be located for the complexes of SCS and SeCSe, while those for SCTe and TeCTe are energetically less stable than the **nL** motifs (by 2 to 3 kJ mol^{-1}), and, thus, are not further discussed.

3.3 Characteristics of blue-shifting hydrogen bonds in linear binding motif

We first investigate the hydrogen bonds found in the linear $F_3CH\cdots OCY$ complexes, whose characteristics of typical blue-shifting hydrogen bonds are exhibited. All of the three systems experience contractions in the C–H bond and the concurrent blue-shifts in its stretching frequencies with comparable magnitudes (Table 3). In particular, the C–H bonds are shortened by approximately 1.2 mÅ, followed by an increase of the associated frequency by 28 to 30 cm^{-1}, of which, the blue-shifting magnitude of OCO and OCS complexes are slightly larger than that of OCSe. The stability as inferred from the complexation interaction energy varies in similar trend, with OCS > OCO > OCSe. It should be noted that, despite their considerably low interactions energies, the magnitudes of C–H contraction and its frequency blue shift are comparable with those in complexes between F_3CH and H_2O.[16,19–21] This trend differs from the increase in proton affinity of the proton acceptors (Table S5, ESI†), while being consistent with the change in $V_{s,min}$ of the electrostatic potential at the proton acceptor (*i.e.*, the O atom), thus, suggesting the electrostatic interactions might play a key role in stabilizing the complexes.

Fig. S9 (ESI†) depicts the topological properties obtained from the AIM analyses for these hydrogen bonding complexes. The topological properties suggest the highly noncovalent

Table 3 Changes in C–H bond lengths in mÅ (1×10^{-3} Å) and their vibrational frequency in cm^{-1} for hydrogen bonding complexes

Complex	Δr_{C-H} (mÅ)	$\Delta \nu_{C-H}$ (cm^{-1})
$F_3CH\cdots OCO$(**L**)	−1.2	29.8
$F_3CH\cdots OCS$(**L**)	−1.2	30.1
$F_3CH\cdots OCSe$(**L**)	−1.1	28.2
$F_3CH\cdots OCO$(**nL-1**)	−0.9	15.4
$F_3CH\cdots OCS$(**nL-1**)	−0.8	13.4
$F_3CH\cdots OCSe$(**nL-1**)	−0.7	12.4
$F_3CH\cdots SCS$(**nL-1**)	−0.1	2.0
$F_3CH\cdots SCSe$(**nL-1**)	0	1.6
$F_3CH\cdots SCTe$(**nL-2**)	0	3.7
$F_3CH\cdots SeCSe$(**nL-3**)	0.2	2.5
$F_3CH\cdots TeCTe$(**nL-3**)	0.4	1.3

nature of these blue-shifting hydrogen bonds. As expected, the hydrogen bonds in linear complexes are characterized by a single bond critical point (BCP) connecting the donor and acceptor atoms (Fig. S9a, ESI†). The electronic properties associated with the BCPs are comparable among $F_3CH\cdots OCY$ complexes with the OCS complex possessing a slightly higher $\rho(r)$ and $\nabla^2\rho(r)$. In particular, those complexes have positive values of $\rho(r) < 0.03$ a.u. and $\nabla^2\rho(r)$, together with ratios of $\frac{-G(r)}{V(r)} > 1$ (Table S6, ESI†); those values fall perfectly into the criteria for noncovalent character of the hydrogen bonds as proposed by Kumar *et al.*[69]

Furthermore, the charge transfer information obtained from NBO analyses (see Table S3, ESI†) demonstrates that the delocalization behaviors in the complexes are virtually identical. The complexes are stabilized by the primary n(O) → σ*(C–H) donations. Additional transfers from electronic densities at n(Y), σ(C–O), and σ(C–Y) to the antibonding orbital σ*(C–H) are also observed. Back donations of about 1 kJ mol^{-1} from σ(C–H)→ σ*(C–O) further stabilizes the complexes. No essential difference was found in the s- and p-characters of the σ(C–H) orbitals.

We further look into the nature of the investigated hydrogen bonds *via* high-order SAPT analyses, from which contributions of physically meaningful energy terms can be evaluated. Shown in Fig. 3(a) is the contributions in percentage of the attractive terms, namely, electrostatics, induction, and dispersion to the attractive interaction energies. The electrostatics and dispersion components primarily stabilize these hydrogen bonding complexes, of which, the former term slightly outweighs. The dispersion interaction becomes more important, while electrostatics contribution declines as the proton acceptor changes from OCO to OCSe. The induction component plays a minor role as it remains below 20% for all complexes. This contribution pattern is in marked distinction with the nonlinear complexes shown in Fig. 3(b), where dispersion plays a dominant role (as discussed later).

From the SAPT results for these complexes at their optimal intermolecular distances, one is tempted to conclude that the electrostatic interaction is the cause of blue-shifts in the C–H frequencies, as suggested by some authors.[20,21] However, it is often argued that the blue-shifting (and red-shifting) behavior is a consequence of a subtle balance between opposing effects.[16,18,19] Therefore, rather than relying on a "single-point" energy decomposition, it is beneficial to understand how the shifting behavior changes as a function of intermolecular distance and how the contributions of energy terms vary accordingly. Fig. 4 presents representative plots of Δr_{C-H} and the contributions of different terms as functions of $r_{C\cdots O}$ for the $F_3CH\cdots OCO$ complex. Interestingly, the C–H bond experiences elongations at large separations, where electrostatic and dispersion interactions dominate, indicating that these two attractive components exhibit bond-lengthening effects. As the $r_{C\cdots O}$ decreases, the lengthening effects diminish; after $r_{C\cdots O}$ = 3.7 Å,

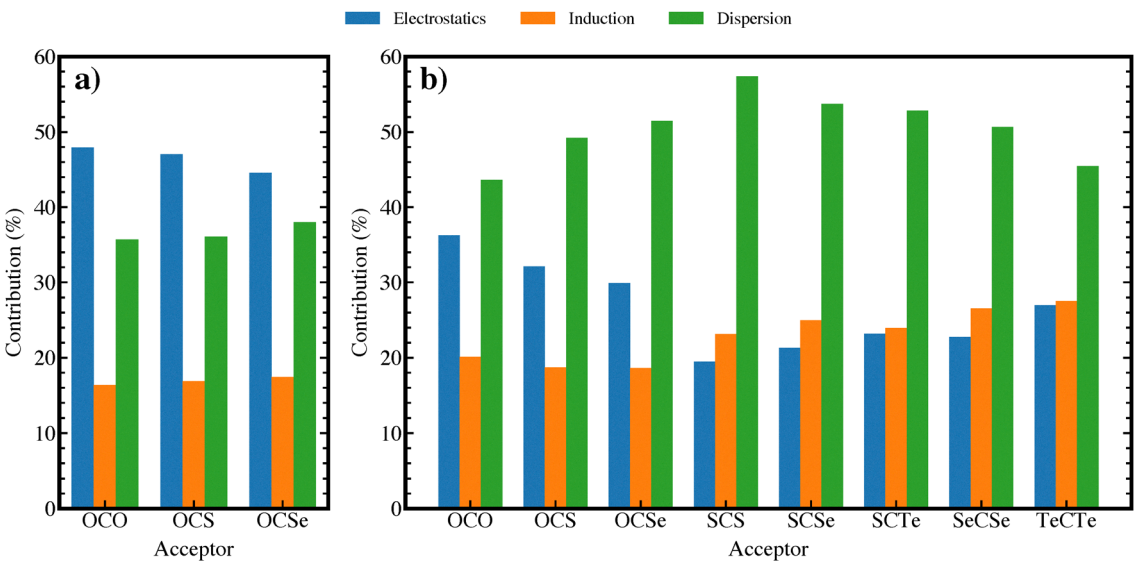

Fig. 3 Contribution of physical terms obtained from SAPT2 + (3)δMP2 calculations for (a) linear hydrogen bonding complexes; (b) nonlinear complexes.

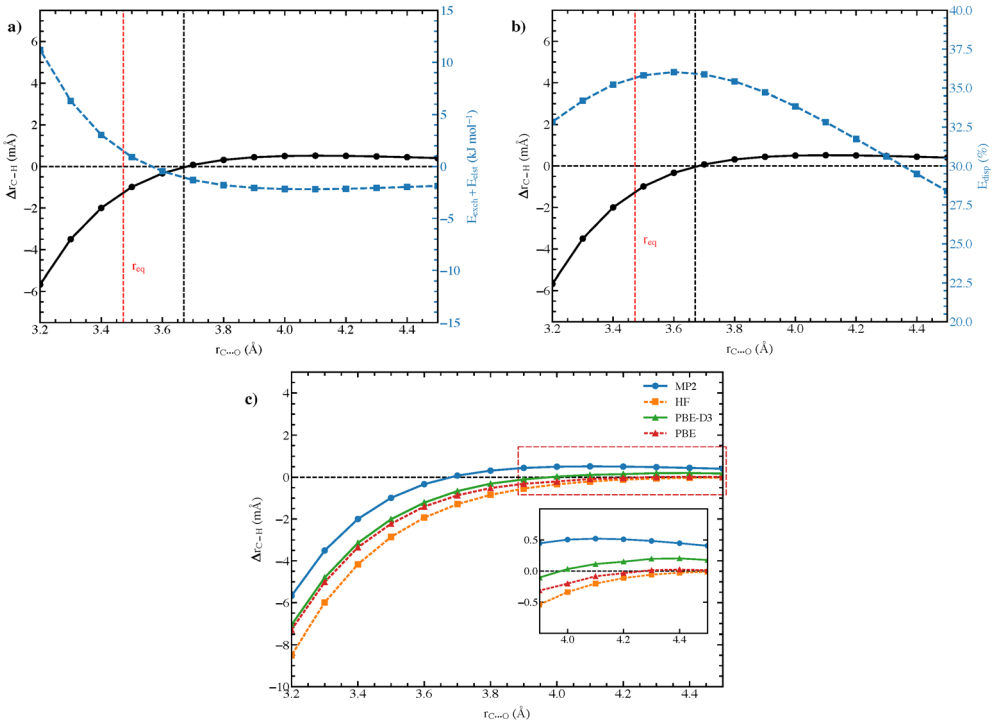

Fig. 4 (a) The changes of C–H bond length and sum of exchange and electrostatics. The red and black dashed lines locate the equilibrium intermolecular C···O distance and the distance at which the C–H bond experiences no-shifting, respectively; (b) the correlation between change in C–H bond length and the contribution in percentage of dispersion interaction as a function of the C···O intermolecular distance; (c) changes in the C–H bond length as functions of intermolecular distance predicted by different methods. A magnified view of the changes in the 3.9–4.5 Å region is given in the inset.

the C–H bond shortens. This behavior is similar to what Mao and Head–Gordon observed for the blue-shifting hydrogen bond systems of $F_3CH\cdots H_2O$ and $F_3CH\cdots NH_3$,[27] while contradicting numerous studies reporting long-range blue-shift phenomena.[20] We find a correlation between the C–H bond shortening and the dominance of exchange repulsive term over its attractive electrostatic counterpart (Fig. 4(a)). This observation suggests that blue-shifting (and red-shifting) hydrogen bonds result from the balance of these interactions, in which the Pauli exchange causes C–H contraction while electrostatics leads to elongation.

Noticeably, as shown in Fig. 4(b), the contribution (in percentage) of dispersion peaks in the region where the C–H bond transitions from lengthening to shortening. As the contribution of dispersion declines at shorter separations, the C–H bond's shortening becomes even more pronounced, suggesting that dispersion might play a slightly more important role than electrostatics in driving red-shift. Indeed, Fig. 4(c) shows that Hartree–Fock (HF) and PBE methods, which do not account for dispersion interaction, fail to reproduce the long-range dispersion-driven elongation. In contrast, with the inclusion the semiempirical D3 dispersion correction, the PBE-D3 successfully mimics the qualitative change of the C–H bond length as observed using the MP2 method. The lengthening role of dispersion explains the reduced blue-shifting behavior observed for the $F_3CH\cdots OCSe$ complex, for which dispersion interaction contributes more than in the other two complexes (Fig. 3(a)).

3.4 Interplay of tetrel bonds and hydrogen bonds

As discussed in Section 3.2, the most stable structures of the $F_3CH\cdots OCY$ complexes involve both hydrogen bonding and tetrel bonding interactions. Different from the hydrogen bond counterparts, the stability of the complexes in this category decreases in the order of OCO > OCS > OCSe. The same order is also observed for the shortening of the C–H bond and the frequency blue-shift, while a reverse trend applies for the lengthening of the C═O bond. We note that the blue-shifting magnitudes in C–H frequencies are less intense in these complexes than in their linear counterparts (see Tables 2 and 3). However, due to collective effects from hydrogen and tetrel bonding interactions, these nonlinear complexes are more stable.

The two types of interactions in these systems are evidently characterized by BCPs from AIM analyses (Fig. S9b, ESI†). Specifically, one BCP is found for the H···O interaction, while two other are located for the tetrel bonding interactions between C–F and π-hole around C atoms of OCY moity, albeit being mistakenly assigned to F···O connections. Additionally, two ring critical points (RCP) are also located (small red balls in Fig. S9b, ESI†). Based on the density properties at the BCPs, these interactions are considered of noncovalent nature, similar to the systems discussed in Section 3.3. Within a given complex, the topological properties are relatively similar among these BCPs (see Table S7, ESI†), of which the hydrogen bonded

BCP has slightly larger $\rho(r)$ and $\nabla^2\rho(r)$ values than those connecting with the tetrel interactions. As Y varies from O to S to Se, the electron density at hydrogen bond BCP increases in the order of OCO < OCSe < OCS, while those of tetrel bond BCPs decreases in a different order of OCO > OCS > OCSe, the latter of which could be explained from the respective $V_{s,max}$ at π-holes around the C atoms (Table 1). The declining tendency in $\rho(r)$ at tetrel bonding BCPs also aligns with the trend in interaction energy of these complexes, suggesting that tetrel bonding interactions plays a more important role than the hydrogen bond in stabilizing the complexes.

Further delocalization properties from NBO analyses suggest that tetrel bonds play the key role in stabilizing the complexes, whereas the contribution of hydrogen bonds is minor. This is evident in large differences in magnitude of tetrel bonding- and hydrogen bonding-involving charge transfers (Table S3, ESI†). In the $F_3CH\cdots OCO$ (**nL-1**), the total charge transfer accounts for a stabilization energy of 3 kJ mol^{-1} for tetrel interactions, of which, 1.4 kJ mol^{-1} comes from the n(F) → π*(C–O) delocalization and 1.6 kJ mol^{-1} from n(O) → σ*(C–F). Meanwhile, the charge transfer of n(O) → σ*(C–H), associated with the hydrogen bonding interaction, is as small as 0.4 kJ mol^{-1}, adding up to a total perturbation energy of 3.4 kJ mol^{-1}. For the OCS analogue, the n(F) → π*(C–S) outweighs n(O) → σ*(C–F) to account for 2.5 kJ mol^{-1} as compared to 0.8 kJ mol^{-1} of the latter. Again, the delocalization associated with hydrogen bonds is minor, which comes from n(O) → σ*(C–H) and the back donation of σ(C–H) → σ*(C–O) of closely similar magnitudes (0.5 and 0.3 kJ mol^{-1}, respectively). The total stabilization energy in this system is 4.2 kJ mol^{-1}. A similar delocalization pattern is also found in the OCSe complex, whose total perturbation energy is nearly the same as of the OCS system. In this system, the C–H involving transfers, albeit being minor, contribute a slightly larger portion to the total energy. The stabilization energy increases in the order of OCO < OCS ≈ OCSe, which is opposing to the trend observed for interaction energy, highlighting that charge transfer is not the sole stabilizing factor in these complexes.

Mo *et al.* suggested that the tendency toward blue-shift would become more considerable if the charge transfer were "turned off".[20] We show here that the $F_3CH\cdots OCY$ complexes do not exactly follow this tendency as the **nL-1** pairs exhibit reduced shortened C–H bond lengths and the corresponding increased frequencies despite their smaller amounts of charge transfer between proton donor and acceptor. However, it should not be excluded that the charge transfers between n(O) and π(C═O) to the remote σ*(C–F) orbitals, which is, in total, of higher magnitude than n(O) → σ*(C–H) shifting, result in structural reorganizations of the proton donor, leading to the increased blue-shifting behavior, as argued by Hobza and coworkers.[15,70] The slightly reduced blue-shifting behaviors in nonlinear complexes, in comparison to their linear counterparts, can be explained by the subtle balance between the two contrasting charge transfer effects.

Fig. 3(b) presents the contributions of energy terms to the attractive interaction energy for the mixed interacting complexes. It is clearly shown that, compared to the linear complexes, dispersion surpasses electrostatics to be the most important interaction, although the change in these interaction's contributions remains across $F_3CH\cdots OCY$ complexes. As speculated in Section 3.3, as Y varies from O to S to Se, the exchange energy well exceed the electrostatics term (with E_{exch} + E_{elst} being 7.4, 8.6, 8.7 kJ mol^{-1}, respectively), suggesting an increase in frequency blue-shift. On the other hand, an increase in contribution of dispersion (as seen in Fig. 3(b)) would lead to an increase in red-shift. As a result of the two opposing effects, a declined blue-shift behavior with marginal magnitudes is observed.

Moreover, a correlation is found between the the elongation undergone by C═O bonds and contribution of attractive terms. Specifically, the C═O bond is increasingly lengthened with decreasing electrostatics and increasing dispersion, suggesting the red-shift effects driven by dispersion forces. The trend in C═O elongation and the underlying driving forces also explain the change in interaction energy across different OCY molecules, which cannot be elucidated from the NBO perspective.

From the above discussion, it could be concluded that the tetrel bonds in the complexes examined in this section, which are largely influenced by electrostatics and dispersion, have a more significant role in the complex's stabilization.

3.5 Non-linear blue-shifting hydrogen bonds

In this section, we aim to elucidate the origin of blue-shifting hydrogen bonds observed in oxygen-free $F_3CH\cdots XCY$ complexes, which take up nonlinear **nL-2** and **nL-3** geometrical motifs. All of these complexes demonstrates the edge between blue- and red-shifting hydrogen bonds with Δr_{C-H} varying from −0.1 to 0.4 mÅ and minimal frequency blue-shift of 1 to 4 cm^{-1}. Based on the vibrational data, we classify the complexes as blue-shifting hydrogen bonds, although it could also be reasonably considered as zero-shifting hydrogen bonds. Generally, the stability increases with the molecular weight of the proton acceptor.

AIM analyses provide a diverse set of topological representations for these complexes (Fig. S9c–e, ESI†). The interactions in $F_3CH\cdots SCS$ and $F_3CH\cdots SCSe$ complexes, which adopt the **nL-1** geometrical motif, are characterized by two topological diagrams that are different from their $F_3CH\cdots OCY$ counterparts. While for OCY complexes, the tetrel bond-related BCPs and the associated bond paths incorrectly suggest F···O interactions, those for SCS and SCSe complexes are found to involve the F···C and F···S interactions, respectively. This inaccurate assignment of tetrel bond BCPs highlights the inconsistency of AIM treatment in predicting bond paths (*i.e.*, interaction lines), which has already been reported elsewhere.[71–73] Meanwhile, the BCPs for H···X are well assigned in all of these systems, at which the $\rho(r)$ value for SCSe complex is marginally larger. Two additional RCPs (small red balls) and a cage critical point are also found for each of the two complexes. For the remaining complexes, the hydrogen bond is characterized by one single BCP, connecting H···C. The electron density and its Laplacian at the BCP increases in the order of SeCSe < SCTe < TeCTe

(Table S9, ESI†). Again, all of the interactions characterized from AIM analyses satisfy the Kumar's criteria to be noncovalent.[69]

NBO results clearly demonstrate hydrogen bonds as the dominant interactions in these complexes (Table S4, ESI†). In the two **nL-1** complexes of SCS and SCSe, the n(S) → σ*(C–H) and n(Se) → σ*(C–H) transfers are the most remarkable delocalizations, with the latter being 1.7 kJ mol^{-1} larger. Back donations of σ(C–H) → π*(C–S) are also found at minimal energies (<0.4 kJ mol^{-1}). On the other hand, the tetrel bonding charge transfer of n(F) → π*(C–S) and n(S/Se) → σ*(C–F) accounts for 2.0 and 1.1 kJ mol^{-1} for the SCS and SCSe complexes, respectively. The geometrical difference also leads to the different in charge transfer pattern. For the remainder, back transfer σ(C–H)→ π*(C–X/Y) becomes more pronounced, making the hydrogen bonding charge transfer the predominant stabilizing factor. Specifically, the total energy of delocalization connected with hydrogen bonds increases from 4.8 to 6.1 to 9.2 kJ mol^{-1}, while those of tetrel bonds make up 1.8, 0.5, and 0.8 kJ mol^{-1} for the SCTe, SeCSe, and TeCTe complexes, respectively. The total perturbation energy from delocalization effects increase in the order of SCS < SeCSe < SCSe ≈ SCTe < TeCTe, which is not the same as the increasing trend in stability.

The interactions in these complexes are characterized by remarkably high dispersion contribution (Fig. 3(b)), which makes up to more than 50% of the total attractive energy (with an exception for TeCTe complex with 45% of dispersion). Notably, the induction interaction becomes the second most important term, leaving electrostatics the least contributing term, albeit the small differences between the two forces.

While it is reasonable to conclude that dispersion primarily drives red-shifting effects (*i.e.*, making blue-shifting less profound), it is difficult to correlate the trend in frequency shift with any energy terms. Interestingly, we find a correlation between the interaction energy and those contributions, as demonstrated in Fig. 5. The (absolute) interaction energy is directly proportional to the contributions of electrostatics and induction, while being inversely proportional to the contribution of dispersion.

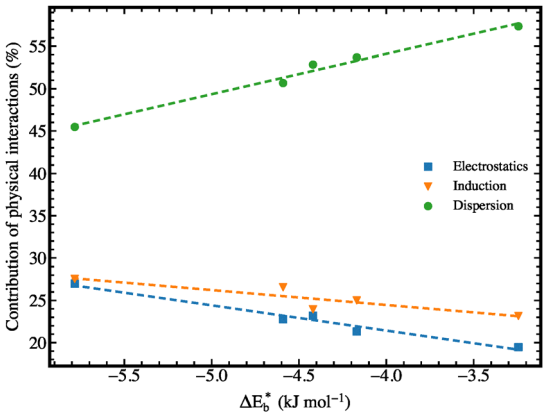

Fig. 5 The correlation between contribution of different physical terms and interaction energy (corrected by ZPE and BSSE) of the $F_3CH\cdots XCY$ complexes.

4 Concluding remarks

In this study, we conducted a theoretical investigation of noncovalent interactions in complexes of fluoroform and carbon dichalcogenides, XCY (where X, Y = O, S, Se, Te). The results were obtained using *ab initio* CCSD(T)/6-311++G(3df,3pd)//MP2/6-311++G(3df,3pd) calculations (aug-cc-pVTZ-PP for Te-containing structures), complemented by AIM, NBO, and SAPT analyses.

The most stable structures across all complexes adopt nonlinear binding motifs. In most cases, tetrel bonds and hydrogen bonds are responsible for stabilization, except for those involving CSe_2, SCTe, and CTe_2, where the hydrogen bond is the sole interaction. All complexes exhibit a series of weak noncovalent interactions, with interaction energy ranging between −6 and −3 kJ mol^{-1}. The C–H bond displays a blue shift in vibrational frequency to varying degrees in all systems.

Among the investigated carbon dichalcogenides, notable distinctions emerge between oxygen-containing and oxygen-free complexes. Specifically, the tetrel bond plays a more prominent role in oxygen-containing complexes, attributed to a higher $V_{s,max}$ around the carbon atoms due to electron-withdrawing nature of oxygen atom. In terms of stability, oxygen-containing systems show a correlation between their stability and $V_{s,min}$ at the proton acceptor in linear hydrogen bonding complexes or $V_{s,max}$ around the carbon atom in the most stable configurations. A linear correlation between electrostatic energy and interaction energy is observed for oxygen-free systems. While dispersion dominates the stabilization of all complexes, two distinct contribution patterns are identified: in oxygen-containing systems, electrostatic interactions play a secondary role, whereas in oxygen-free systems, they are the least attractive component.

Detailed analyses of the linear blue shifting $F_3CH\cdots OCY$ (Y = O, S, Se) complexes reveal that red shifts are primarily long-range phenomena, whereas blue-shifts occur at shorter distances. These trends can be attributed to the competing effects of the red-shift-driving electrostatic attraction and the blue-shift-driving exchange repulsion, with the latter dominating near the equilibrium region. Dispersion interactions are also found to act as a red-shift-causing factor and likely also play a role in the long-range red shift behavior.

Author contributions

TNH: conceptualization, investigation, methodology, analysis, writing – original draft; NTMN: implementation, investigation, writing – review and editing; BDA: implementation, writing – review and editing; NTT: conceptualization, supervision, writing – review and editing, funding acquisition.

Conflicts of interest

There are no conflicts to declare.

Data availability

The data supporting this article have been included as part of the ESI.†

Acknowledgements

This research was funded by the Vietnam National Foundation for Science and Technology Development (NAFOSTED) under grant number 104.06-2023.49.

References

1 Z. Derewenda, U. Derewenda and P. Kobos, *J. Mol. Biol.*, 1994, **241**, 83–93.
2 G. R. Desiraju, *Acc. Chem. Res.*, 1996, **29**, 441–449.
3 M. Wahl, *Trends Biochem. Sci.*, 1997, **22**, 97–102.
4 P. Auffinger and E. Westhof, *J. Mol. Biol.*, 1997, **274**, 54–63.
5 Y. Mandel-Gutfreund, H. Margalit, R. L. Jernigan and V. B. Zhurkin, *J. Mol. Biol.*, 1998, **277**, 1129–1140.
6 O. Takahashi, Y. Kohno and M. Nishio, *Chem. Rev.*, 2010, **110**, 6049–6076.
7 G. R. Desiraju, *Nature*, 2001, **412**, 397–400.
8 R. D. Bach, C. Thorpe and O. Dmitrenko, *J. Phys. Chem. B*, 2002, **106**, 4325–4335.
9 S. Horowitz and R. C. Trievel, *J. Biol. Chem.*, 2012, **287**, 41576–41582.
10 Z. Berkovitch-Yellin and L. Leiserowitz, *Acta Crystallogr., Sect. B: Struct. Sci.*, 1984, **40**, 159–165.
11 G. R. Desiraju, *Acc. Chem. Res.*, 1991, **24**, 290–296.
12 E. Cubero, M. Orozco, P. Hobza and F. J. Luque, *J. Phys. Chem. A*, 1999, **103**, 6394–6401.
13 P. Hobza and Z. Havlas, *Chem. Phys. Lett.*, 1999, **303**, 447–452.
14 Y. Gu, T. Kar and S. Scheiner, *J. Am. Chem. Soc.*, 1999, **121**, 9411–9422.
15 P. Hobza and Z. Havlas, *Chem. Rev.*, 2000, **100**, 4253–4264.
16 X. Li, L. Liu and H. B. Schlegel, *J. Am. Chem. Soc.*, 2002, **124**, 9639–9647.
17 K. Hermansson, *J. Phys. Chem. A*, 2002, **106**, 4695–4702.
18 I. V. Alabugin, M. Manoharan, S. Peabody and F. Weinhold, *J. Am. Chem. Soc.*, 2003, **125**, 5973–5987.
19 J. Joseph and E. D. Jemmis, *J. Am. Chem. Soc.*, 2007, **129**, 4620–4632.
20 Y. Mo, C. Wang, L. Guan, B. Braïda, P. C. Hiberty and W. Wu, *Chem. – Eur. J.*, 2014, **20**, 8444–8452.
21 C. Wang, D. Danovich, S. Shaik and Y. Mo, *J. Chem. Theory Comput.*, 2017, **13**, 1626–1637.
22 S. Scheiner and T. Kar, *J. Phys. Chem. A*, 2002, **106**, 1784–1789.
23 N. T. Trung, T. T. Hue and M. T. Nguyen, *J. Phys. Chem. A*, 2009, **113**, 3245–3253.
24 H. Q. Dai, N. N. Tri, N. T. Thu Trang and N. T. Trung, *RSC Adv.*, 2014, **4**, 13901–13908.
25 N. T. An, N. Vu Thi and N. T. Trung, *Phys. Chem. Chem. Phys.*, 2024, **26**, 22775–22789.
26 L. T. Tu Quyen, B. N. Tung, P. N. Thach, N. N. Tri and N. T. Trung, *RSC Adv.*, 2024, **14**, 14114–14125.
27 Y. Mao and M. Head-Gordon, *J. Phys. Chem. Lett.*, 2019, **10**, 3899–3905.
28 S. Scheiner, *CrystEngComm*, 2021, **23**, 6821–6837.
29 T. Steiner, *J. Mol. Struct.*, 1998, **447**, 39–42.
30 M. Domagała, S. J. Grabowski, K. Urbaniak and G. Mlostoń, *J. Phys. Chem. A*, 2003, **107**, 2730–2736.
31 M. Domagała and S. J. Grabowski, *J. Phys. Chem. A*, 2005, **109**, 5683–5688.
32 S. Wojtulewski and S. J. Grabowski, *Chem. Phys.*, 2005, **309**, 183–188.
33 M. Domagała and S. J. Grabowski, *Chem. Phys.*, 2010, **367**, 1–6.
34 B. R. Beno, K.-S. Yeung, M. D. Bartberger, L. D. Pennington and N. A. Meanwell, *J. Med. Chem.*, 2015, **58**, 4383–4438.
35 R. Reddi, K. K. Singarapu, D. Pal and A. Addlagatta, *Mol. BioSyst.*, 2016, **12**, 2408–2416.
36 N. T. Trung, P. N. Khanh, A. J. P. Carvalho and M. T. Nguyen, *J. Comput. Chem.*, 2019, **40**, 1387–1400.
37 S. Ghosh, P. Chopra and S. Wategaonkar, *Phys. Chem. Chem. Phys.*, 2020, **22**, 17482–17493.
38 H. A. Fargher, T. J. Sherbow, M. M. Haley, D. W. Johnson and M. D. Pluth, *Chem. Soc. Rev.*, 2022, **51**, 1454–1469.
39 W. Lv, Y. Xu, T. Yang, L. Wang, J. Huang, H. Huang and G. Feng, *J. Chem. Phys.*, 2024, **160**, 134302.
40 M. Iwaoka and S. Tomoda, *J. Am. Chem. Soc.*, 1994, **116**, 4463–4464.
41 M. Iwaoka, H. Komatsu and S. Tomoda, *Bull. Chem. Soc. Jpn.*, 1996, **69**, 1825–1828.
42 S. J. Narayanan, B. Sridevi, T. K. Chandrashekar, A. Vij and R. Roy, *Angew. Chem., Int. Ed.*, 1998, **37**, 3394–3397.
43 A. J. Mukherjee, S. S. Zade, H. B. Singh and R. B. Sunoj, *Chem. Rev.*, 2010, **110**, 4357–4416.
44 P. Chopra and S. Chakraborty, *Chem. Phys.*, 2018, **500**, 54–61.
45 L. M. Azofra and S. Scheiner, *J. Chem. Phys.*, 2015, **142**, 034307.
46 P. N. Khanh, C. D. Phan, D. Q. Ho, Q. Van Vo, V. T. Ngan, M. T. Nguyen and N. T. Trung, *J. Comput. Chem.*, 2018, **40**, 464–474.
47 M. Hou, Z. Liu and Q. Li, *Int. J. Quantum Chem.*, 2020, **120**, e26251.
48 S. Anila and C. H. Suresh, *Phys. Chem. Chem. Phys.*, 2019, **21**, 23143–23153.
49 M. P. Hoffman and S. S. Xantheas, *J. Am. Chem. Soc.*, 2025, **147**, 11152–11171.
50 P. Ramasami and T. A. Ford, *Mol. Phys.*, 2014, **112**, 683–693.
51 P. Ramasami and T. A. Ford, *J. Mol. Struct.*, 2014, **1072**, 28–31.
52 P. Ramasami and T. A. Ford, *J. Mol. Model.*, 2015, **21**, 35.

53 J. Del Bene, J. Elguero and I. Alkorta, *Molecules*, 2018, **23**, 906.
54 M. Moradkhani and Y. A. Tyula, *Mol. Phys.*, 2024, **122**, e2313037.
55 M. J. Frisch, G. W. Trucks, H. B. Schlegel, G. E. Scuseria, M. A. Robb, J. R. Cheeseman, G. Scalmani, V. Barone, G. A. Petersson, H. Nakatsuji, X. Li, M. Caricato, A. V. Marenich, J. Bloino, B. G. Janesko, R. Gomperts, B. Mennucci, H. P. Hratchian, J. V. Ortiz, A. F. Izmaylov, J. L. Sonnenberg, D. Williams-Young, F. Ding, F. Lipparini, F. Egidi, J. Goings, B. Peng, A. Petrone, T. Henderson, D. Ranasinghe, V. G. Zakrzewski, J. Gao, N. Rega, G. Zheng, W. Liang, M. Hada, M. Ehara, K. Toyota, R. Fukuda, J. Hasegawa, M. Ishida, T. Nakajima, Y. Honda, O. Kitao, H. Nakai, T. Vreven, K. Throssell, J. A. Montgomery, Jr., J. E. Peralta, F. Ogliaro, M. J. Bearpark, J. J. Heyd, E. N. Brothers, K. N. Kudin, V. N. Staroverov, T. A. Keith, R. Kobayashi, J. Normand, K. Raghavachari, A. P. Rendell, J. C. Burant, S. S. Iyengar, J. Tomasi, M. Cossi, J. M. Millam, M. Klene, C. Adamo, R. Cammi, J. W. Ochterski, R. L. Martin, K. Morokuma, O. Farkas, J. B. Foresman and D. J. Fox, *Gaussian~16 Revision A.03*, Gaussian Inc., Wallingford CT, 2016.
56 P. Pracht, S. Grimme, C. Bannwarth, F. Bohle, S. Ehlert, G. Feldmann, J. Gorges, M. Müller, T. Neudecker, C. Plett, S. Spicher, P. Steinbach, P. A. Wesołowski and F. Zeller, *J. Chem. Phys.*, 2024, **160**, 114110.
57 C. Bannwarth, S. Ehlert and S. Grimme, *J. Chem. Theory Comput.*, 2019, **15**, 1652–1671.
58 N. T. T. Cuc, N. T. An, V. T. Ngan, A. K. Chandra and N. T. Trung, *RSC Adv.*, 2022, **12**, 1998–2008.
59 N. T. An, N. T. Duong, N. N. Tri and N. T. Trung, *RSC Adv.*, 2022, **12**, 35309–35319.
60 S. Boys and F. Bernardi, *Mol. Phys.*, 1970, **19**, 553–566.
61 T. Lu, *J. Chem. Phys.*, 2024, **161**, 082503.
62 R. F. W. Bader, *Chem. Rev.*, 1991, **91**, 893–928.
63 T. A. Keith, *AIMAll (Version 19.10.12)*, 2019, **https://aim.tkgristmill.com**.
64 A. E. Reed, L. A. Curtiss and F. Weinhold, *Chem. Rev.*, 1988, **88**, 899–926.
65 D. G. A. Smith, L. A. Burns, A. C. Simmonett, R. M. Parrish, M. C. Schieber, R. Galvelis, P. Kraus, H. Kruse, R. Di Remigio, A. Alenaizan, A. M. James, S. Lehtola, J. P. Misiewicz, M. Scheurer, R. A. Shaw, J. B. Schriber, Y. Xie, Z. L. Glick, D. A. Sirianni, J. S. OBrien, J. M. Waldrop, A. Kumar, E. G. Hohenstein, B. P. Pritchard, B. R. Brooks, H. F. Schaefer, A. Y. Sokolov, K. Patkowski, A. E. DePrince, U. Bozkaya, R. A. King, F. A. Evangelista, J. M. Turney, T. D. Crawford and C. D. Sherrill, *J. Chem. Phys.*, 2020, **152**, 184108.
66 C.-T. Phan Dang, N. M. Tam, T.-N. Huynh and N. T. Trung, *RSC Adv.*, 2023, **13**, 31507–31517.
67 S. Emamian, T. Lu, H. Kruse and H. Emamian, *J. Comput. Chem.*, 2019, **40**, 2868–2881.
68 E. S. Kryachko and T. Zeegers-Huyskens, *J. Phys. Chem. A*, 2001, **105**, 7118–7125.
69 N. Kumar, S. Saha and G. N. Sastry, *Phys. Chem. Chem. Phys.*, 2021, **23**, 8478–8488.
70 B. J. van der Veken, W. A. Herrebout, R. Szostak, D. N. Shchepkin, Z. Havlas and P. Hobza, *J. Am. Chem. Soc.*, 2001, **123**, 12290–12293.
71 A. Haaland, D. J. Shorokhov and N. V. Tverdova, *Chem. – Eur. J.*, 2004, **10**, 4416–4421.
72 J. Poater, M. Solà and F. M. Bickelhaupt, *Chem. – Eur. J.*, 2006, **12**, 2889–2895.
73 J. Poater, R. Visser, M. Solà and F. M. Bickelhaupt, *J. Org. Chem.*, 2007, **72**, 1134–1142.